Additive Manufacturing 36 (2020) 101604

Contents lists available at ScienceDirect

Additive Manufacturing

journal homepage: www.elsevier.com/locate/addma

Improved high cycle fatigue performance of additively manufactured 17-4 PH stainless steel via in-process refining micro-/defect-structure

P.D. Nezhadfar [a,b], Kathryn Anderson-Wedge [c], S.R. Daniewicz [c], Nam Phan [d], Shuai Shao [a,b], Nima Shamsaei [a,b,*]

[a] Department of Mechanical Engineering, Auburn University, Auburn, AL, 36849, USA
[b] National Center for Additive Manufacturing Excellence (NCAME), Auburn University, Auburn, AL, 36849, USA
[c] Department of Mechanical Engineering, University of Alabama, Tuscaloosa, AL, 35487, USA
[d] Structures Division, Naval Air Systems Command (NAVAIR), Patuxent River, MD, 20670, USA

ARTICLE INFO

Keywords:
Laser beam powder bed fusion (LB-PBF)
Fatigue behavior
Fatigue crack growth
Microstructure refinement
Porosity

ABSTRACT

The usage of an appropriate shield gas for laser beam powder bed fusion (LB-PBF) of the popular 17−4 precipitation hardened (PH) stainless steel (SS) has long been debated in the additive manufacturing (AM) community. While the inertness of Ar is often desirable as the shield gas from unwanted chemical reactions, its low solubility combined with the violent nature of the melt pool inevitably result in the formation of defects that are detrimental to the fatigue performance of the alloy. On the other hand, although N_2 is reactive with some alloys (e.g. titanium), it may have remarkable favorable effects on the mechanical properties and fatigue performance of 17−4 PH SS. In this article, the advantageous effects of N_2 as an in-process micro-/defect-structure refiner of LB-PBF 17−4 PH SS, and in turn, an enhancer of its mechanical/fatigue properties are demonstrated. It is shown that, compared to Ar, the use of N_2 shield gas induces more retained austenite, refines grains, makes the melt pools deeper, produces fewer and smaller pores, and as a result, slightly improves tensile properties, moderately improves crack growth resistance, and considerably improves axial fatigue properties in the high cycle regime.

1. Introduction

The Fe-17Cr-4Ni-4Cu precipitation hardening (PH) stainless steel (SS), often dubbed as 17−4 PH SS, is a martensitic hardenable SS with a desirable combination of strength, ductility, fatigue strength, fracture toughness, and high corrosion resistance, depending on the post-manufacture heat treatment applied. This cost-effective SS often finds use in key engineering, defense, and energy sectors [1]. Additive manufacturing (AM) is advantageous over conventional subtractive manufacturing techniques in applications requiring the fabrication of near-net shaped parts with more complex geometries [2]. Therefore, there is a strong incentive in the industry to adopt AM in the fabrication of 17−4 PH SS parts to further benefit from this material's appealing properties.

The repetitious melting-solidification cycles inherent to typical AM processes result in elevated defect content and complex microstructure that are difficult to remediate and hard to predict [3,4]. The defects serve as stress risers and compromise mechanical performance, especially in fatigue critical applications [5]. Such defects include volumetric ones, e.g. gas entrapped pores and lack-of-fusion (LoF) defects, and surface roughness, with the latter being very detrimental to the fatigue performance of additively manufactured (AM) parts in their as-built surface condition [6]. Further, the variability in defects' morphology, population, and distribution as well as the surrounding microstructure, exacerbate the uncertainty in the fatigue performance of AM parts [7,8]. While the goal to fabricate high-density components eliminating the occurrence of defects may be desirable, these imperfections may be inherent to the AM processes and persist even under the most optimum operating conditions. Given this inevitability, establishing the

Abbreviations: AM, Additive manufacturing/Additively manufactured; BCC, Body centered cubic; BCT, Body centered tetragonal; CA, Condition A; CT, Compact tension; EBSD, Electron backscatter diffraction; ECCI, Electron channeling contrast imaging; FCC, Face centered cubic; FCG, Fatigue crack growth; FCGR, Fatigue crack growth rate; CMOD, Crack mouth opening displacement; FIB, Focused ion beam; HCF, High cycle fatigue; HIP, Hot isostatic pressing; HT, Heat treated; IPF, Inverse pole figure; LB-PBF, Laser beam powder bed fusion; LCF, Low cycle fatigue; LoF, Lack of fusion; NHT, Non-heat treated; PH, Precipitation hardening/hardened; SEM, Scanning electron microscope/microscopy; SS, Stainless steel; TD, Transverse direction.

* Corresponding author at: Department of Mechanical Engineering, Auburn University, Auburn, AL, 36849, USA.
E-mail address: Shamsaei@auburn.edu (N. Shamsaei).

https://doi.org/10.1016/j.addma.2020.101604
Received 7 June 2020; Received in revised form 21 August 2020; Accepted 12 September 2020
Available online 21 September 2020

Nomenclature

b	Fatigue strength exponent
M_s	Start martensite transformation temperature
N_f, $2N_f$	Cycles to failure, Reversals to failure
R_ε	Ratio of minimum to maximum strain
% RA	Percent reduction in area
α'	Martensite
γ	Austenite
σ'_f	Fatigue strength coefficient
σ_a	Stress amplitude
σ_m	Mean stress
σ_y	Yield strength
σ_f	True fracture stress
σ_u	Ultimate tensile strength
ε_f	True fracture strain
ε_{max}	Maximum strain
ε_{min}	Minimum strain
ε_a	Total strain amplitude
$\frac{\Delta\varepsilon_p}{2}$	Plastic strain amplitude
$\frac{\Delta\varepsilon_e}{2}$	Elastic strain amplitude

process-structure-property-performance relationships is therefore essential to expedite the adoption of AM (such as laser beam powder bed fusion (LB-PBF) method) 17−4 PH SS [9,10].

As in the case for all AM metallic materials, the microstructure and defect characteristics in AM 17−4 PH SS (which govern their mechanical performance) are dictated by the solidification dynamics and thermal history. For instance, porosities are formed due to the gas entrapment in the melt pool as a result of a high cooling/solidification rate [2]. Indeed, owing to heat accumulation (thus larger melt pools and longer solidification time for gas bubbles to escape), porosity levels were shown to decrease in larger LB-PBF 17−4 PH SS components [11]. The LoF defects are formed when there is an insufficient melt pool overlap either between layers, or between intralayer tracks [11,12], which can be affected by the changes in the part geometry, manufacturing process parameters, etc.

As for microstructure, although the stable phase at room temperature is body centered tetragonal (BCT) martensite, the as-fabricated 17−4 PH SS via LB-PBF may include a martensite (~60−90%) + austenite (~10−40%) phase composition [6,13]. This is generally due to the compositional heterogeneity (especially the distribution of austenite stabilizer elements such as Ni, Cu, Mn, etc.) induced by rapid solidification. The tetragonality of the BCT lattice is closely related to the carbon content, i.e. $c/a = 1 + 0.046C$, where C is in wt.%. In the case of 17−4 PH SS, as the carbon content is extremely low—0.01 %, the lattice is often reported as body centered cubic (BCC) [14].

In the microstructure typically reported in the literature for LB-PBF 17−4 PH SS, the morphology of the as-solidified, columnar prior-δ grains are visible [15]. In fact, the well-known lath morphology of the martensite phase is not obvious and the microstructure is sometimes reported as ferritic microstructure (by-passing the formation of austenite, and therefore, absence of martensite) [15]. Many studies reported that a heat treatment at 1050 °C for 30 min can fully homogenize the composition (reaching Condition A) and, if low-temperature aging is followed, can lead to a relatively uniform, fully martensitic microstructure [6,16]. However, this heat treatment cannot alter the prior-δ morphology, and upon over-aging, the austenite tends to nucleate at the prior-δ grain boundaries [17]. The parameters whose influence on AM materials' microscopic features, and consequent mechanical properties have been studied so far include powder condition (i.e. chemical composition [18], recyclability [19,20] atomization media [21]), process parameters [22], geometry and size of the parts [11,23], and post processing [6].

Shield gas is another process parameter that can significantly impact the solidification and thermal history of AM SSs and was found influential in altering the microstructure as well as porosity levels of materials [24–27]. The appropriate shield gas for LB-PBF 17−4 PH SS is perhaps among the most debated topics in the AM community [26,28,29]; however, mostly focusing on the static mechanical properties such as hardness and tensile strength. The most popular shield gas types for the LB-PBF 17−4 PH SS appear to be Ar and N_2 [30]. However, systematic investigations regarding the process-structure relationships seem to exist predominantly in research related to laser welding, which has an affinity to laser AM [31–33]. Relevant knowledge (K) in the area can be summarized below:

K1) Compared to Ar, N_2 has good solubility in molten high-Cr SS (3.4×10^{-5} wt. %), and the large (mm sized) N_2 bubbles, formed during laser welding, can be dissolved quickly (within 30 μs) into the melt pool [34]. Utilization of N_2, therefore, reduces the tendency for porosity formation [34,35].

K2) Dissolved N in the steel, which tends to exist as interstitial atoms in the octahedral site of a face center cubic (FCC) parent lattice [36], is a potent austenite stabilizer [13]. Indeed, N_2 has been reported to accelerate the ferrite to austenite phase transformation during solidification resulting in less δ-ferrite retained in the microstructure [31,37]. In addition, N-doped alloys can overcome the strength-ductility trade-off due to the capability of N element to produce hierarchical, heterogeneous fine-grain microstructure [38].

K3) In response to fiber laser excitation (wavelength ~ 1 μm, a popular wavelength among metal AM machines), stainless steels typically produce similar weakly ionized metal plumes under the shielding of either Ar or N_2 gases [39,40]. When the shield gas flow is inadequate, the laser is significantly attenuated by the plume [25]. On one hand, the laser attenuation reduces the direct energy input to the melt pool, which can alleviate the formation of keyholes. On the other hand, the laser attenuation in the plume heats the shield gas, which can serve to heat the materials/powder around the melt pool, and as a result, lead to larger melt pools and reduced gas entrapped pores.

K4) N_2 has higher thermal conductivity (~40 % higher) and molar heat capacity (50 % higher) as compared to Ar [30,41]. Assuming the same flow rate for N_2 and Ar gases, on one hand, this results in a more efficient convection heat transfer between the melt pool and N_2 shield gas and a higher cooling rate [30]. On the other hand, such properties of N_2 favor the heat transfer from the metal plume to the shield gas (see K3), which then releases the absorbed energy to the surrounding surface [40,42]. N_2 shield gas can, therefore, lead to a higher laser energy absorption, and as a result, formation of larger melt pools, better overlap of the melt pools in subsequent layers as well as the adjacent tracks within a layer. This should reduce the formation tendency for LoF defects.

K5) During LB-PBF, N_2 gas reacts with Cr in the molten metal and forms Cr_2N nano-precipitates, which has been well known to serve as a strong inhibitor of grain growth [43–45]. These nano precipitates may also serve as heterogeneous nucleation sites for solid phase during solidification [38]. Therefore, the microstructure of LB-PBF 17−4 PH SS specimens fabricated under N_2 atmosphere is anticipated to be finer compared to the ones under Ar.

Given the facts listed above, N_2 shield gas may be an appealing candidate for LB-PBF 17−4 PH SS to realize in-process refinement of microstructure and defects, leading not only to better static mechanical properties, but also enhanced fatigue performance. Fatigue damage of materials commonly occurs in three main stages: I. crack initiation, II.

crack propagation, and III. final fracture. Fatigue behavior of materials, depending on the applied stress levels, can be roughly divided into two regimes, i.e. low cycle fatigue (LCF) regime ($N_f < 10^4$ cycles), and high cycle fatigue (HCF) regime ($N_f > 10^5$ cycles).

In the LCF regime, fatigue life is dominated by crack propagation (Stage II) which is strongly influenced by the amount of crack-tip plastic deformation [5,46]. The anticipated improvements in ductility (due to higher retained austenite content and less internal defects) afforded by the utilization of N_2 shield gas as opposed to Ar, may improve the crack growth resistance of the LB-PBF 17−4 PH SS. Increase in strength without sacrifice in ductility, in other words, increase in tensile toughness, is known to improve the fracture toughness of materials that undergo ductile failure [46]. In the HCF regime, the fatigue life is governed by the initiation of fatigue cracks, which is strongly influenced by the presence of defects (including gas entrapped pores and LoF defects) for machined LB-PBF 17−4 PH SS [11]. As N_2 tends to reduce the defect levels, the N_2-shielded LB-PBF 17−4 PH SS, is expected to outperform their Ar-shielded counterparts in HCF regime.

The present study attempts to achieve the in-process refinement of microstructure and defects in LB-PBF 17−4 PH SS via the use of N_2 shield gas as an alternative to Ar, and, through which, demonstrate an enhanced fatigue performance. The authors also aim to shed light on the effect of shield gas types, N_2 versus Ar, on the microstructure, porosity state, melt pool geometry, and their consequent results on the fatigue performance of LB-PBF 17−4 PH SS. For the first time to the authors' knowledge, the effect of shield gas type on the fatigue crack initiation and growth behavior of LB-PBF 17−4 PH SS is revealed. This article is organized as follows: in Section 2, the experimental design of this study is delineated in detail. In Section 3, the experimental results, including microstructural (Section 3.1) and mechanical (Section 3.2) properties, are presented along with their immediate observations. The findings of this study are further discussed in section 4, where the observed variations in fatigue behaviors due to the utilization of N_2 shield gas, as opposed to Ar, are attributed to microstructural and defect characteristics. Finally, conclusions are drawn in Section 5.

2. Experimental procedures

2.1. Material and specimen fabrication

The chemical composition of 17−4 PH SS powder used in this study is listed in Table 1. The pre-alloyed and argon-atomized powder was provided by LPW Technology Inc. with the powder particle size within the range of 15−45 μm.

An EOS M290 machine (an LB-PBF system) with 400 W Yb (Ytterbium) fiber laser and with a wavelength of 1060 nm was utilized to fabricate all 17−4 PH SS specimens. The employed main process parameters for fabricating 17−4 PH SS under Ar shield gas suggested by EOS are listed in Table 2. To understand the effect of shield gas type, the same process parameters were used to fabricate parts under N_2 shield gas. It is worth noting that the gas flow rate was the same for both shield gases, and the scan strategy utilized was a conventional parallel scan with a 67° interlayer rotation.

The design of experiment is detailed in Table 3. Two sets of $11.5 \times 11.5 \times 77\ mm^3$ square bars were fabricated in the vertical direction and machined to the round axial fatigue specimens with a uniform gage section, shown in Fig. 1(a). All the machined specimens were further hand polished to remove the machining marks and make the surface mirror-finished. The surface roughness of the gage section was measured after polishing to be $R_a = 0.93 \pm 0.24\ \mu m$ using Keyence VHX6000, a digital optical microscope. It must be mentioned that the tensile tests were performed using the same geometry. Two sets of walls with the dimension of $65 \times 6.5 \times 65\ mm^3$ were fabricated vertically and further machined by electrical discharge machining (EDM) into compact tension (CT) specimens in Fig. 1(b), following ASTM E647 standard [47]. For each type of specimens (i.e. axial fatigue and CT), one set was fabricated under Ar shield gas (dubbed "Ar specimens"), and one set of specimens was fabricated under N_2 shield gas (dubbed "N_2 specimens").

All the axial fatigue and CT specimens were subjected to CA-H1025 heat treatment procedure (solution heat treating at 1050 °C for 0.5 h followed by air cooling (Condition A, or CA), then aging at 552 °C for four hours followed by air cooling (H1025) [6]) utilizing a box furnace in an Ar atmosphere to prevent oxidation and surface decarburization. Some non-heat treated specimens were reserved for microstructural analysis and tensile tests to examine the as-fabricated properties. The gage section of all the fatigue specimens was further polished using P320-P4000 grit sandpapers to remove all the machining marks. To track each set of specimens throughout the article, figures, and tables, HT-Ar and HT-N_2 are the designations used for the heat treated (HT), and NHT-Ar and NHT-N_2 are used for the non-heat treated (NHT) specimens fabricated in Ar and N_2 atmospheres, respectively. Besides, the red color in figures is assigned to N_2 specimens and blue color represents Ar specimens.

Table 2
The process parameters for LB-PBF 17-4 PH SS suggested by EOS.

Laser power (W)	Scanning speed (mm/s)	Hatch distance (μm)	Layer thickness (μm)
220	755.5	100	40

Table 3
Design of experiment: number of specimens under each build specifications.

Specimen type	Ar shield gas	N_2 shield gas	Build dimensions
Axial fatigue/tensile	18	18	$11.5 \times 11.5 \times 77\ mm^3$
Compact tension (CT)	4	4	$65 \times 6.5 \times 65\ mm^3$

2.2. Microstructure characterization

To characterize the microstructure, samples were first cut from the gage section of the specimens parallel to the build direction. Specimen preparation and microstructural analysis were carried out based on the ASTM E3−11 standard [48]. For optical microscopy, the microstructure was revealed using Beraha's tint reagent. Microstructural characterization and any measurement (i.e. pore size, melt pool size, grain size) were carried out employing Keyence VHX6000, a digital optical microscope, and a Zeiss Crossbeam 550 focused ion beam scanning electron microscope (FIB-SEM). The microstructure also was studied using electron backscatter diffraction (EBSD) and electron channeling contrast imaging (ECCI).

2.3. Mechanical testing

Tensile and uniaxial fully-reversed strain-controlled fatigue tests were conducted using an MTS landmark servohydraulic testing machine with 100 kN load cells. In order to measure the strain at the gage section, an MTS mechanical extensometer was utilized. Regarding the tensile tests, to avoid any damage to the extensometer which has a limited

Table 1
Chemical composition of 17-4 PH SS powder, provided by LPW Technology Inc.

	C	Cr	Ni	Cu	Mn	Si	Nb	Mo	N	O	P	S	Fe
(Wt. %)	0.01	15.6	4.03	3.89	0.24	0.29	0.33	<0.01	0.01	0.05	0.004	0.003	Bal.

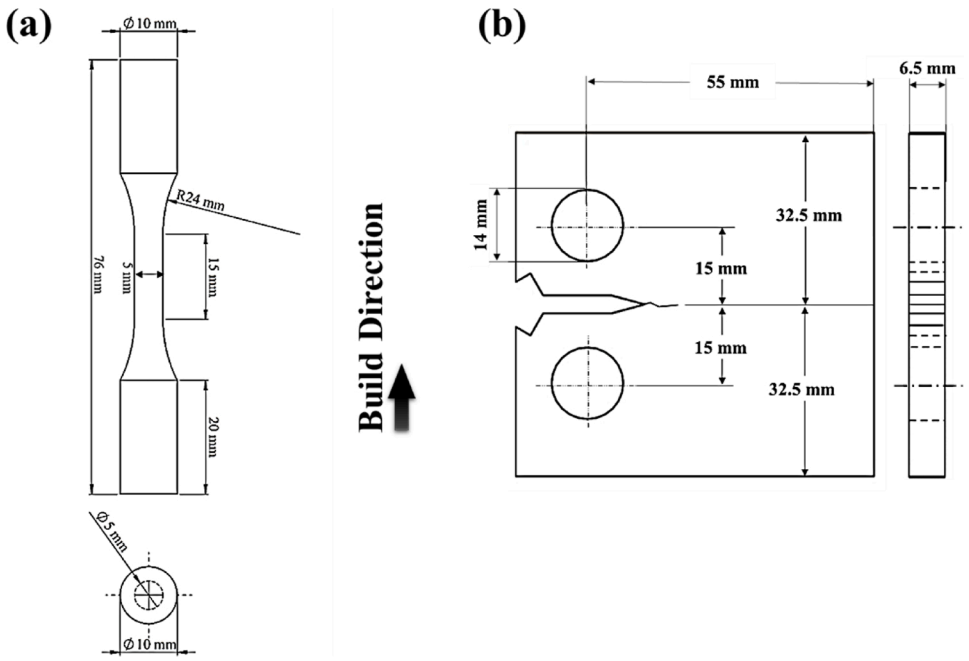

Fig. 1. Drawings of (a) round axial fatigue specimens with a uniform gage section, and (b) compact tension (CT) specimens following ASTM E647 standard [47].

travel distance, tests were performed in two consecutive steps, i.e. a strain-controlled and displacement-controlled steps. Tensile tests were started first under strain-controlled mode up to a 0.045 mm/mm strain, paused to remove the extensometer, and then switched to displacement-controlled mode until fracture. For certainty of the results, two tensile tests were conducted for each condition, and the results were fairly consistent. There were limited specimens available for tensile testing, therefore, the averaged values are reported for comparison; these results are not to be used as materials data for the design/qualification purposes.

Room-temperature, uniaxial fully-reversed ($R_\varepsilon = \varepsilon_{min}/\varepsilon_{max}$ = -1) strain-controlled fatigue tests were performed based on ASTM E606 standard [49] at constant strain amplitudes within the range of 0.002−0.004 mm/mm. To maintain a similar average cyclic strain rate throughout all the tests, frequencies were attuned for each test based on the applied strain amplitude. A sinusoidal waveform was applied until failure (complete separation) or up to 10^7 reversals, which was considered 'run-out' in this study. It is worth noting that all strain-controlled fatigue tests were stopped after a few thousand cycles and switched to the force-controlled mode since no pronounced macroscopic plastic strain was observed during the fatigue tests performed in this study.

The low-stress fatigue crack growth (FCG) tests were carried out on CT specimens under load-control at room temperature with a sinusoidal loading waveform with a load ratio of $R = 0.1$ and frequency of $f = 10$ Hz until fracture. It is worth noting that there will not be a crack tip plastic zone size disparity to overcome since the pre-cracking loading was the same as the one applied for FCG rate testing. Load amplitudes ranged from 4275 N to 1575 N (the first test was started with higher load amplitude to initiate the crack, however, as the confidence was obtained that the crack would initiate, the load amplitude level was reduced for further tests). It is worth mentioning that the load ratio, *R*, remained constant (R = 0.1) for all the tests, therefore, change in the load amplitude should not have any influence on the FCG rate. FCG rate, da/dN, and stress intensity factor ranges, ΔK, were determined using the recorded crack mouth opening displacement (CMOD) values, load range, and the measured cycle count. Pre-cracking was conducted up to a length of 11−14 mm to achieve a corresponding initial ΔK value of approximately 10 MPa$\sqrt{}$m. To ensure the consistency of the results, FCG tests were repeated 3 times for each processing condition.

To study the factors responsible for fatigue crack initiation and failure mechanisms in LB-PBF 17−4 PH SS specimens, fractography analysis was performed using SEM. Before fractography analysis, the fracture surfaces were cut using a precision cutter, sonicated in water and alcohol solution, and then washed using acetone to eliminate any moisture and dirt that may be present on the fracture surfaces.

3. Experimental results

In this section, the experimental observations on the in-process induced microstructure and defects refinement in LB-PBF 17−4 PH SS, and the related favorable variations in mechanical properties, due to the use of N_2 as shield gas, are presented. Specifically, the effect of shield gas change from Ar to N_2 on the phase constituent (i.e. martensite, austenite, etc.), grain sizes, melt pool geometry (i.e. depth, and overlap depth), and porosity size and number are inspected. The resulting mechanical properties (i.e. tensile, FCG, and fatigue) of LB-PBF 17−4 PH SS specimens are also presented. In this section, only the experimental results, and corresponding to which, the immediate observations and brief discussion are made. The relationships between the shield gas type and micro-/defect-structure, as well as the relationships between the micro-/defect-structure and mechanical properties, are formally established in Section 4.

3.1. Microstructural observations

3.1.1. Grain size, morphology, and phases

Fig. 2 shows a schematic of an axial fatigue specimen and the sample for microstructure characterization cut from the gage section, which was cross-sectioned parallel to the build direction. The EBSD inverse pole figure (IPF) maps in the direction normal to the cross-sections (i.e. along the Z direction) for the non-heat treated specimens are presented in Fig. 2. The apparent grain shapes on the cross-sections of both NHT-N_2 (Fig. 2(a)) and NHT-Ar (Fig. 2(b)) specimens are "U" shaped, dictated by the solidification history unique to track-by-track and layer-by-layer fabrication strategy in AM. In fact, the grains are grown epitaxially along the heat dissipation path, center of the melt pool, toward the build plate during fabrication [37].

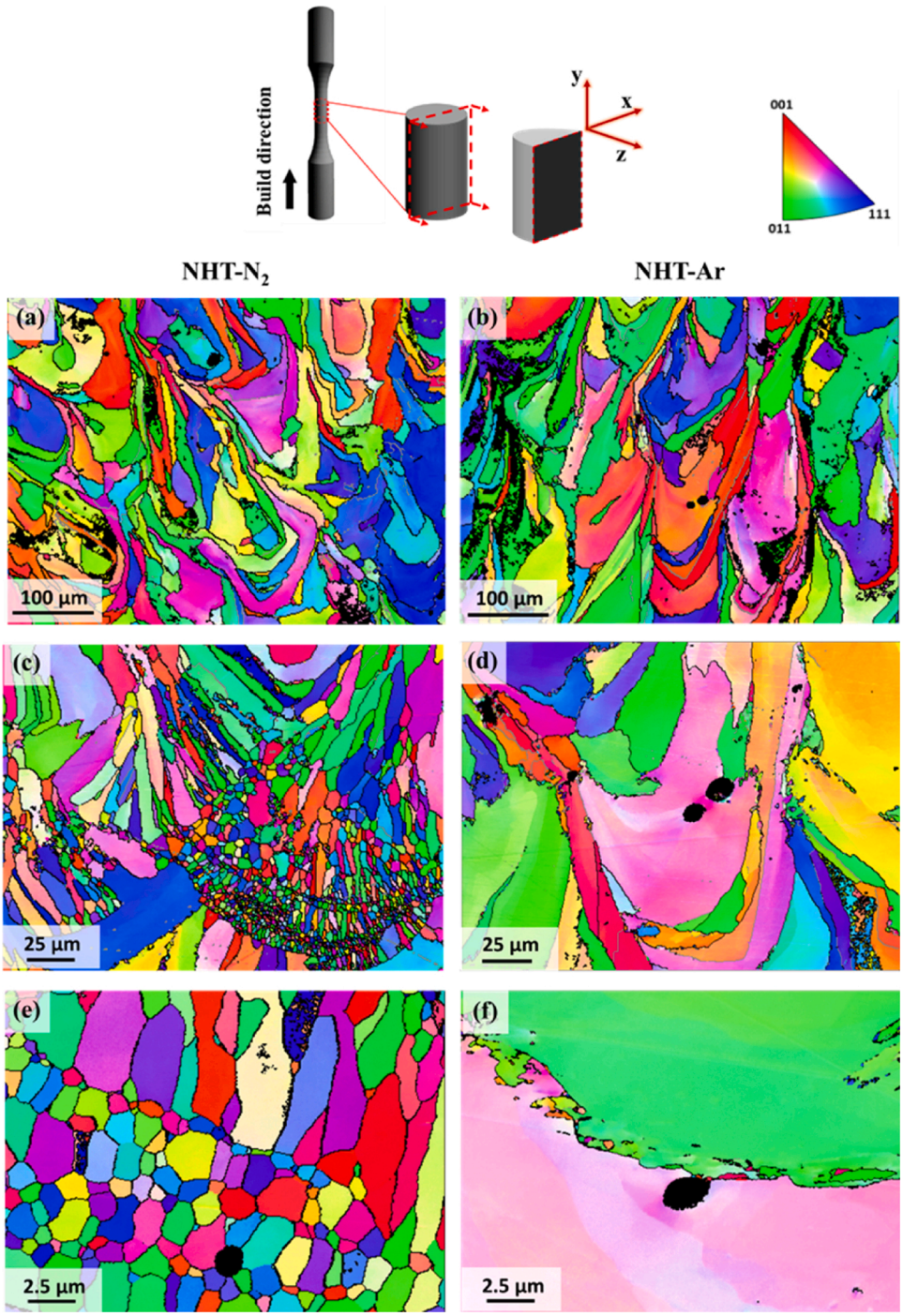

Fig. 2. A schematic of axial fatigue specimen and the cross-sectioned plane parallel to the build direction in the gage section for microstructure characterization, and the EBSD results for NHT LB-PBF 17-4 PH SS specimens: (a), (c), (e) IPF NHT-N_2, and (b), (d), (f) IPF NHT-Ar.

It can be seen in IPF maps for both NHT-N_2 and NHT-Ar specimens that the grains appear to be randomly oriented (i.e. there is not any preferred grain orientation) and must be noted that they do not resemble the typical morphology of the lath martensite, albeit martensite being the stable phase in the room temperature. According to Alnajjar et al. [15], these grains are δ ferrites, which could be the result of fast cooling. They reported that fast cooling through the γ-stable temperature range by-passes the γ phase and δ ferrite retains at room temperature. As expected, a small fraction (1 %) of retained austenite was detected by EBSD in the cross-sectioned plane of NHT-N_2 specimens (N is a strong austenite stabilizer as was mentioned in K2 in the introduction), while there was no retained austenite detected in NHT-Ar specimens. According to the Fe-Cr-N phase diagrams [50], the Cr concentration of 15.6 wt. % (Table 1), an increase of 50 ppm N in the material can stabilize the austenite in the microstructure. Therefore, using the N_2 shielding gas increases the possibility of the dissolution of N in the material, which in conjunction with the effect of other elements such as Cu, Ni, and Mn, stabilizes the austenite, and results in the austenite retainment to the room temperature (K1 and K2 mentioned in the introduction).

In addition, it appears that the grains are finer in NHT-N_2 specimen as compared to those of NHT-Ar one. A closer look into the microstructure, there are islands of equiaxed ultra-fine grains in the NHT-N_2 specimen (Fig. 2(c) and (e)), while the grains are coarse and elongated in

the NHT-Ar condition (Fig. 2(d) and (f)). The equiaxed ultra-fine grains are mostly found around the spherical gas entrapped pores in NHT-N_2 specimens. As summarized in the introduction in K1 and K5, N_2 can be rapidly dissolved into the melt pool [41,51], the atomic N then forms nitrides (mostly Cr_2N), which either prevents grain growth or acts as heterogeneous nucleation sites during solidification [38,43]. The average grain size for NHT-N_2 and NHT-Ar were found based on EBSD results to be 5.4 ± 1 μm and 15.5 ± 2.3 μm, respectively.

Fig. 3(a) and (b) show the mosaic of consecutive EBSD IPF maps of the vertical cross-sections (same orientation as the ones exposed in Fig. 2) of the HT-N_2 and HT-Ar specimens, respectively. The microstructure of the heat treated specimens is clearly lath martensitic. It appears from the IPF maps that the martensitic laths in the HT-N_2 specimens are finer than those in the HT-Ar ones. The exact lath thickness is quantified in Section 4.1 using high-resolution ECCI. There is also a finite fraction of austenite retained in HT-N_2 condition (1%) in the inspected cross-sectioned plane after heat treatment, while the HT-Ar specimens have fully martensitic microstructure.

3.1.2. Melt pools

In order to investigate the effect of shield gas type on the melt pool dimensions, specimens were cross-sectioned perpendicular to the known laser scan direction and parallel to the build direction, on the most top layer, as is schematically presented in Fig. 4. The very top layer does not get re-melted, and therefore, the melt pool can be fully revealed. The cross-sections were polished and etched to reveal the melt pool boundaries for both NHT-N_2 and NHT-Ar specimens (Fig. 4(a) and (b)). Recently, NASA has proposed a methodology [12] for melt pool analysis based on the ratios between the melt pool depth (d_p) and the layer thickness (t_L), as well as between the overlap depth (d_0) to t_L, i.e. d_p/t_L and d_0/t_L, respectively. In fact, the above-mentioned ratios show how deep the melt pools are, and whether the overlap of the melt pools is sufficient to avoid the formation of LoF defects. Accordingly, the melt pool depths and overlap depths were measured for N_2 and Ar specimens and the results are presented in Fig. 4(a), (b), and (c).

As seen, both the average melt pool depth and overlap depth are higher for the specimens fabricated under N_2 as compared to the ones fabricated under Ar shield gas, indicating larger melt pools. The d_p/t_L and d_0/t_L ratios are 3.5 and 2.3 for NHT-N_2 specimens, while they are 3.1 and 1.9 for NHT-Ar ones. Higher values of d_p/t_L and d_0/t_L ratios for N_2 specimens are less favorable, respectively, for the formation of gas entrapped pores and LoF defects, as compared to Ar specimens. The slightly deeper melt pools evident in the NHT-N_2 specimens can be explained by the better laser energy absorption associated with the use of N_2 shield gas (as summarized in Points K3 and K4 in the introduction), resulting in lower overall cooling/solidification rates, which permits more time for the pores to escape.

3.1.3. Defects

Fig. 5 shows the typical porosity distribution of specimens fabricated under both shield gases in the cross-sectional plane parallel to the build direction (see Fig. 2) in the gage section. The red dashed lines in Fig. 5(a) and (b) indicate the depth to which the surface machining is performed for all tensile and axial fatigue specimens. It is evident that the pores in the N_2 specimens (Fig. 5(a)) are not only smaller in population, but also smaller in size compared to those in the Ar specimens (Fig. 5(b)). This is supported by the statistical analysis presented in Fig. 5(c) for the square bars and Fig. 5(d) for the gage section after machining, which have been performed on 5 polished sections (including the ones shown in Fig. 5(a) and (b)). It is worth noting that the specimens used for defect analysis were selected from the same location on the build plate of N_2 and Ar prints.

The fewer and finer pores in the N_2 specimens can be associated with the larger melt pools as well as the better solubility of N_2 than Ar in the metal (Points K1, K3, and K4 as summarized in the introduction). The better solubility may result in shrinkage of the pores as N can dissolve in the material [51–53]; therefore, pores become smaller in size. In addition, considering the lower cooling/solidification rates in N_2 specimens as compared to those of Ar specimens, the gas pores in the melt pool have more opportunity to escape [11,54], resulting in less gas entrapped pores in N_2 specimens (see Fig. 4(c)). The larger melt pools observed in the N_2 specimens are believed to be the result of the better laser energy absorption when N_2 is used as shield gas (Points K3 and K4), which overcomes any additional convention cooling effects imposed by N_2.

3.2. Mechanical properties

3.2.1. Tensile results

Fig. 6 shows the monotonic tensile behavior of LB-PBF 17−4 PH SS fabricated under N_2 and Ar shield gases in both non-heat treated and heat treated conditions. In addition, the details of tensile properties obtained for each condition are listed in Table 4 and compared to those of the wrought counterpart undergone the same heat treatment (i.e. CA-H1025). Due to limited specimens tested, it must be noted that the results are only for comparison and not for design purposes. Fig. 6(a) shows the engineering stress-strain curve in the strain-controlled portion of the tensile test up to 0.045 mm/mm strain, and Fig. 6(b) represents the engineering stress-displacement curve of the displacement-

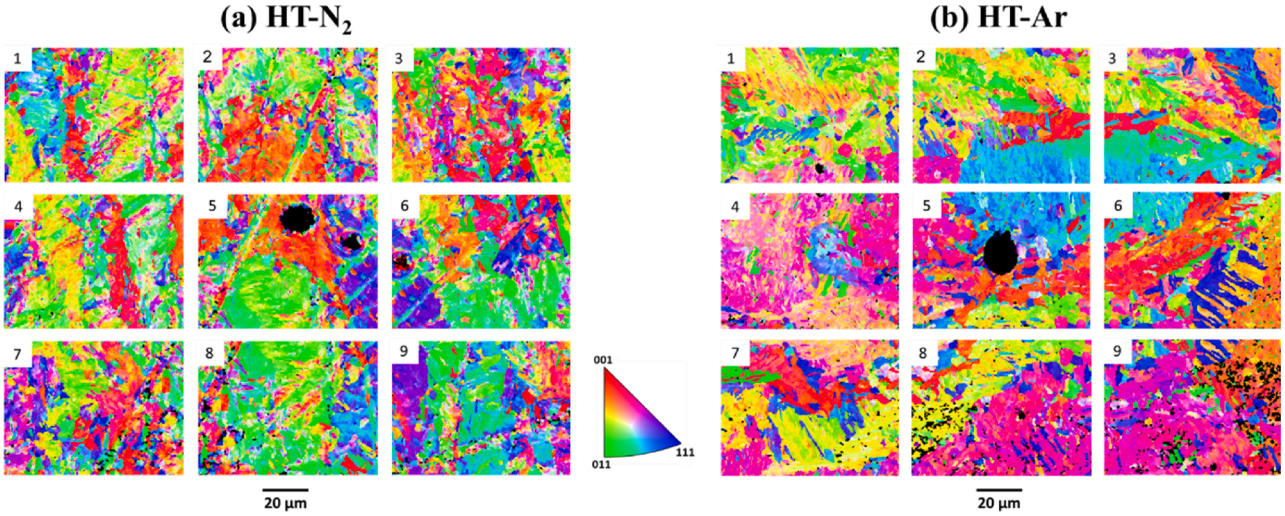

Fig. 3. IPF maps of heat treated LB-PBF 17-4 PH SS specimens on the cross-sectioned plane parallel to the build direction: (a) HT-N_2, and (b) HT-Ar.

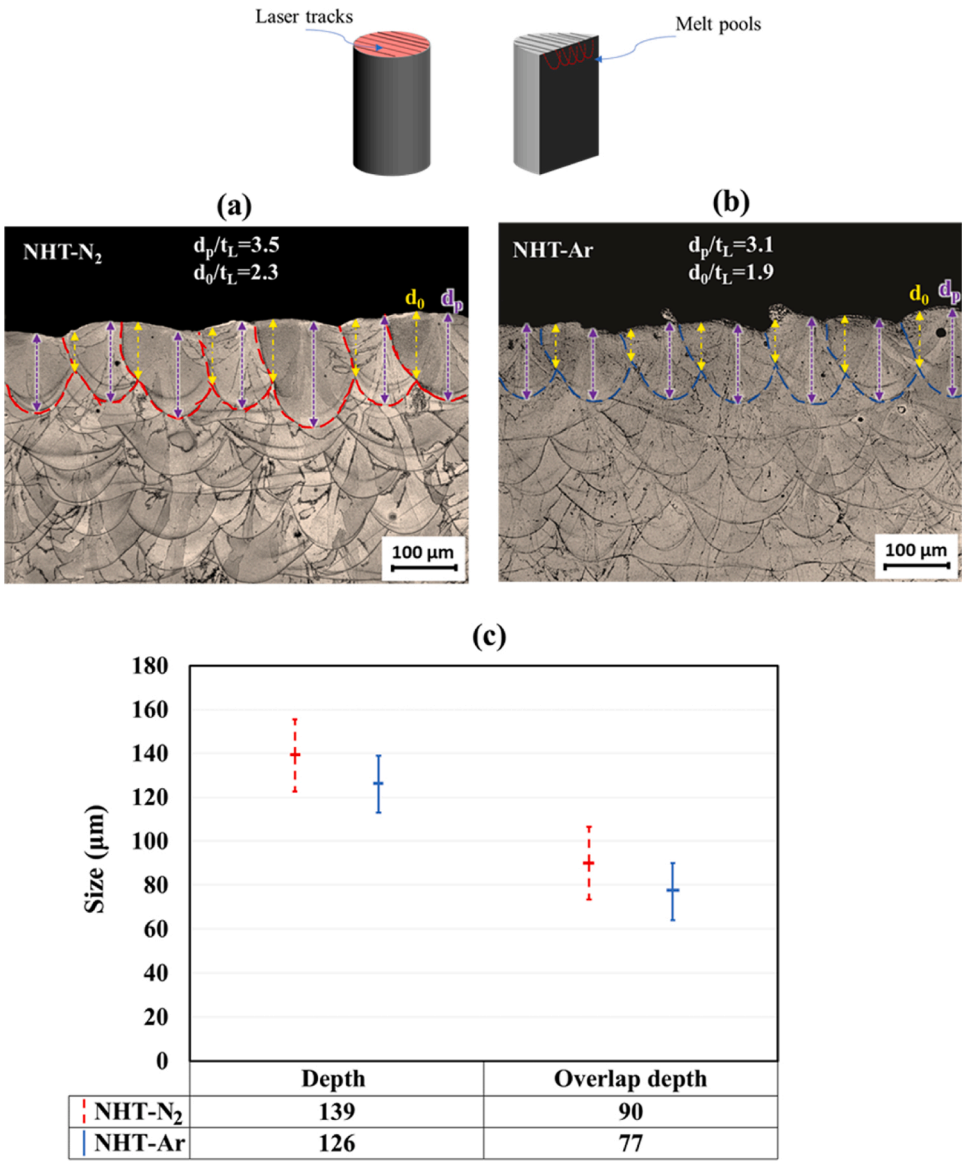

Fig. 4. Post-built melt pool size measurement; the schematic is showing the last printed layer with laser track direction. (a) Melt pool shape/size in NHT-N_2 specimens, (b) melt pool shape/size in NHT-Ar specimens, and (c) measured melt pool depths and overlap depths.

controlled portion of the test, all the way up to fracture. It must be mentioned that the Bridgman correction factor was employed to account for the stress triaxiality imposed by necking to obtain the true fracture stress [5].

As reported in Table 4, regardless of the shield gas type, the heat treated LB-PBF 17−4 PH SS specimens exhibit substantially higher yield strength (σ_y) than their wrought counterparts in the same heat treatment condition [55]. This is attributed to the finer microstructure produced by the AM process as compared to the conventional manufacturing method [6]. As is evident in Fig. 6 (see solid curves) and Table 4, the non-heat treated LB-PBF 17−4 PH SS specimens fabricated in N_2 (NHT-N_2) has higher σ_y, σ_f, and ε_f than the Ar ones (NHT-Ar). This increase in tensile strength (σ_y, andσ_f) can be ascribed to the grain refinement (see Fig. 2). The improvement in ductility may be associated with the less porosity formed in N_2 specimens (see Fig. 5(d)) [56]. Besides, the presence of retained austenite in the microstructure may enhance the ductility of the material; first, austenite is softer than the martensite and can accommodate more plastic deformation [57]. Second, stacking faults can be formed in austenite during deformation and lead to martensite transformation induced plasticity increasing the ductility of the material [58].

After heat treatment, the HT-N_2 specimens possess slightly higher σ_y and ε_f, but lower σ_f than the HT-Ar ones. The increase in σ_y seen for HT-N_2 specimens is attributed to the finer microstructure, however, this might have decreased the potential for strain hardening and consequently resulted in lower σ_f than HT-Ar specimens. Moreover, the presence of austenite can affect the strength of heat treated 17−4 PH SS in two ways. First, austenite itself is softer and more ductile compared to the martensite. Second, Cu as an austenitic stabilizer dissolves easily in austenite phase, which reduces the Cu fraction in martensite, and consequently, lessens the precipitation hardening effect of Cu [16,26]. Therefore, it is not expected that N_2-shielded material to have significantly higher tensile strength than the Ar-shielded counterparts, as evident in the tensile data generated in this study. The slight increase in ductility for HT-N_2 specimens may be due to the less porosity formed as well as the presence of retained austenite in HT-N_2 specimens [26].

3.2.2. *Fatigue crack growth (FCG) results*

The FCG behavior of LB-PBF 17−4 PH SS specimens fabricated under Ar and N_2 shield gases and undergone CA-H1025 heat treatment

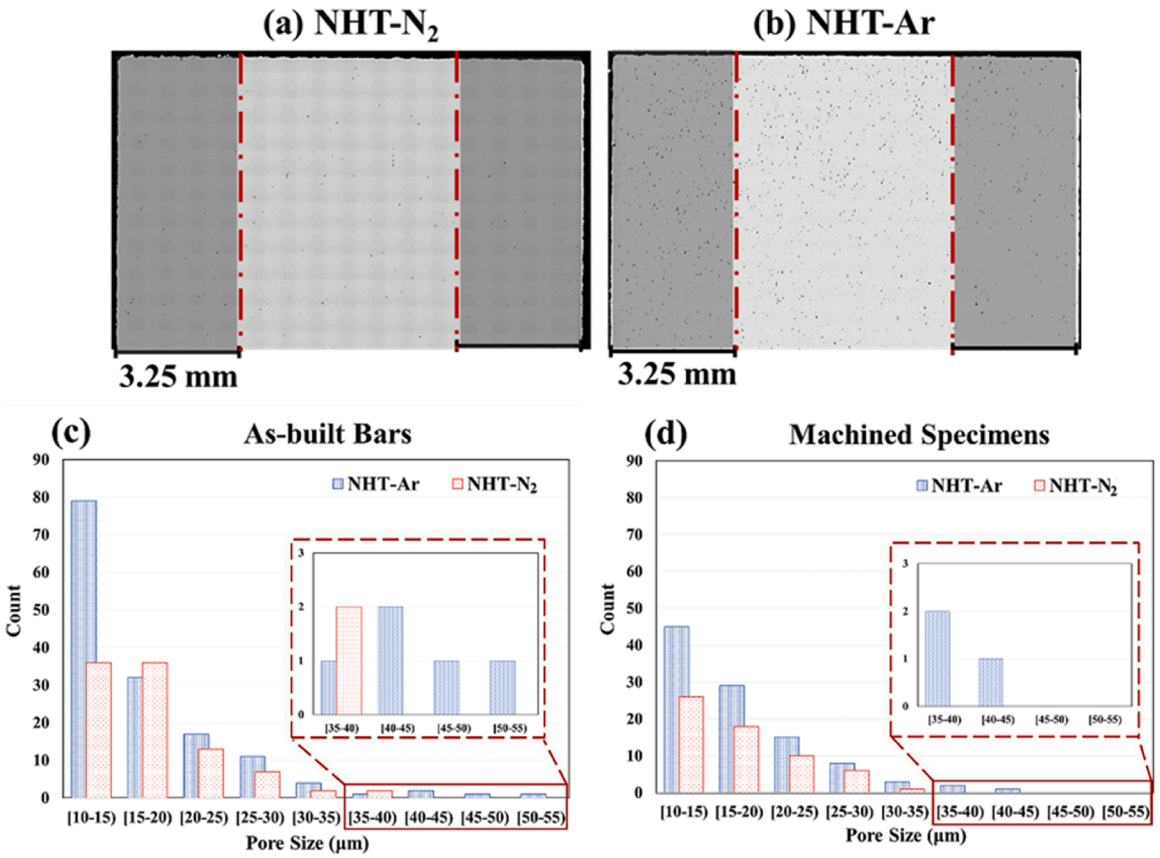

Fig. 5. Porosity distribution in a cross-sectional plane parallel to the build direction for (a) NHT-N_2 and (b) NHT-Ar specimens. The statistical distribution of the pore size in NHT-N_2 and NHT-Ar specimens in (c) as-built bars, and (d) gage section of the machined specimens. Note that the shaded area in (a) and (b) indicate the portion that was removed by machining for all the tensile and axial fatigue specimens.

procedure (i.e. the HT-Ar and HT-N_2 specimens) are compared in Fig. 7. As seen, the HT-N_2 specimens exhibit lower fatigue crack growth rate (FCGR) near the threshold regime (i.e. Regime I) shown in Fig. 7(b) as compared to that of HT-Ar ones. The finer microstructure and the consequential increased resistance to slip in HT-N_2 may have contributed to the slower growth of the microstructurally small cracks, which is governed by slip. The higher porosity level (larger and more pores) and the associated stress concentrations in Ar specimens may also have increased their FCGR and resulted in lower ΔK_{th} values as compared to the N_2 specimens. In the Paris regime (i.e. Regime II), HT-N_2 specimens possess a slightly higher slope as compared to the HT-Ar counterparts; the FCG rates of HT-N_2 and HT-Ar specimens become nearly identical toward the end of Regime II (Fig. 7(c)). By fitting the data in the Paris regime to the Paris equation:

$$\frac{da}{dN} = A(\Delta K)^n \quad (1)$$

where A and n are the y-intercept and slope of the line, respectively), the fitting parameters shown in Table 5 are obtained for each condition. In Regime III, the HT-N_2 specimens exhibit higher cyclic fracture toughness as compared to the HT-Ar ones, which may be attributed to the substantially lower population of volumetric defects in HT-N_2 specimens, as shown in Fig. 5.

3.2.3. Axial fatigue results

Fig. 8 presents the stabilized hysteresis loops of fully-reversed strain-controlled fatigue tests for HT-N_2 (Fig. 8(a)) and HT-Ar ((Fig. 8(b)) LB-PBF 17−4 PH SS specimens. As seen, irrespective of the shield gas type, LB-PBF 17−4 PH SS shows very little to no macroscopic plastic deformation under the applied strain amplitudes in this study. This has been also reported for LB-PBF 17−4 PH SS undergone other heat treatment conditions [6].

Table 6 summarizes the results of axial fatigue tests, including strain amplitude, ε_a, stress amplitude, σ_a, mean stress, σ_m, and reversals to failure, $2N_f$, for HT-N_2 and HT-Ar conditions.

It is noted that the tensile/compressive mean stresses were calculated to be around, and in most cases, less than 5% of the respective stress amplitude; hence, they should not have affected the fatigue behavior. Fig. 9(a) and (b) compare, respectively, the strain-life and stress-life fatigue behavior of LB-PBF 17−4 PH SS specimens fabricated under N_2 and Ar shield gases and heat treated following the CA-H1025 schedule. It is evident that the HT-N_2 specimens in general exhibit a better fatigue performance at both LCF and HCF regimes and almost at all strain levels. As shown in Fig. 9, two out of three HT-N_2 specimens were run-out at 0.0025 mm/mm strain amplitude, while only one out of four HT-Ar specimens reached the run-out defined in this study. The only failure of the HT-N_2 specimen at 0.0025 mm/mm strain amplitude occurred at a substantially higher life than the HT-Ar failed specimens (by at least a factor of four). As elastic behavior dominated the fatigue performance (Fig. 8), the Basquin equation, given below [5], was used to obtain the stress-life fatigue properties (i.e. fatigue strength coefficient, $\sigma_f^{'}$, and fatigue strength exponent, b, for each condition):

$$\sigma a = \sigma_f^{'}(2Nf)^b \quad (2)$$

Accordingly, the linear least square fit method using the Basquin's equation in a semi log-log scale was used to obtain the fatigue parameters, σ'_f and b, for HT-N_2 and HT-Ar specimens (see Fig. 9(b)). It is worth noting that the run-out data were excluded to obtain the best fitting results. The results are listed in Table 7, noting that the data at the run-out level were excluded to obtain the best fit.

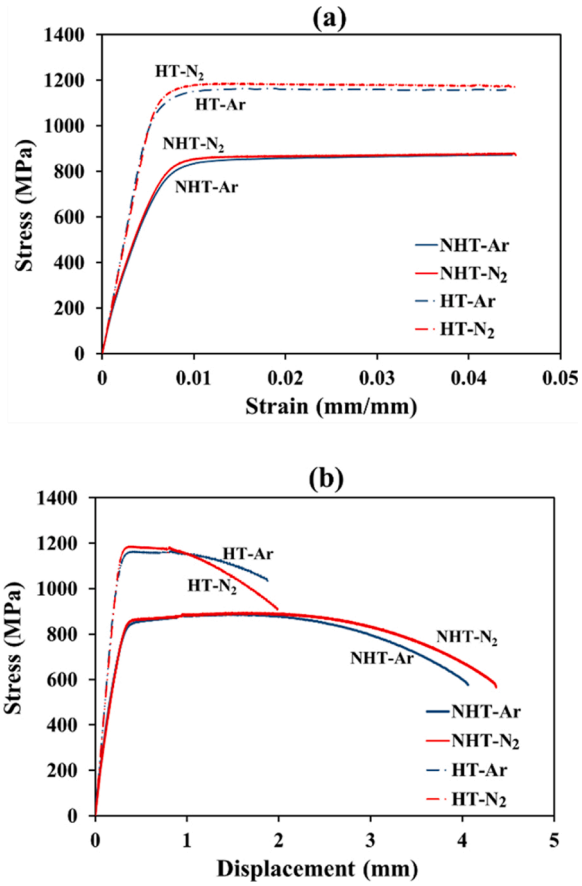

Fig. 6. Monotonic tensile behavior of LB-PBF 17-4 PH SS specimens fabricated under Ar and N_2 shield gases for both NHT and HT conditions: (a) strain-controlled up to 0.045 strain, and (b) displacement-controlled after removing the extensometer up to fracture.

Table 4
Monotonic tensile properties of LB-PBF 17-4 PH SS fabricated under Ar and N_2 shield gases in both NHT and HT conditions, as well as wrought 17-4 PH SS in CA-H1025 condition [55]. σ_y – yield stress (proof stress at 0.01 of strain), σ_f – true fracture stress (corrected for necking), RA% - area reduction at fracture, and ε_f – true fracture strain.

Fabrication method	Heat treatment	σ_y (MPa)	σ_f (MPa)	RA %	ε_f (mm/mm)
LB-PBF	NHT-N_2	855	900	49	0.66
	NHT-Ar	840	887	46	0.61
	HT-N_2	1178	1192	33	0.39
	HT-Ar	1150	1238	26	0.30
Wrought	CA-H1025 [55]	1000	N/A	N/A	N/A

4. Discussion on experimental results

In this section, the enhancement in mechanical properties (including the tensile, axial fatigue, and FCG behavior) of the LB-PBF 17−4 PH SS due to the use of N_2 shield gas instead of Ar is comprehensively discussed and correlated with the refined microstructure and defects, including grain size, melt pool geometry, and porosity size and distribution.

4.1. Tensile behavior as affected by micro-/defect-structures

As expected, and also in agreement with the literature, performing heat treatment increases the strength of the LB-PBF 17−4 PH SS. This can be attributed to the formation of nano-size Cu-rich precipitates (the size of only several nm) [30,59] and the formation of fine lath martensitic structure which reduces the mean free path of dislocations, limiting the ductility of the materials [30,60]. Indeed, as the strength increases, the ductility of the specimens significantly decreases, i.e. from a fracture strain of ~0.65 to ~0.35 (see Table 4).

The utilization of N_2 shield gas does impose favorable effects on the tensile properties of LB-PBF 17−4 PH SS, although the effects on the true fracture stress are overwhelmed by the effect of the heat treatment. Specifically, due to the use of N_2 shield gas, both the yield strength, σ_y, and ductility, ε_f, of the heat treated and non-heat treated specimens noticeably improved, as is evident in Fig. 6 and Table 4. The NHT-N_2 and HT-N_2 specimens respectively possess 0.05 and 0.09 higher strain at fracture than NHT-Ar and HT-Ar ones (Table 4). This is consistent with the higher cyclic fracture toughness for the HT-N_2 specimens than HT-Ar ones observed during the FCG tests in Fig. 7.

The slightly increased ductility in HT-N_2 specimens as compared to the HT-Ar ones can be attributed to more retained austenite stabilized by the dissolved N atoms (summarized in Point K2 in the introduction) and less and smaller volumetric defects formed in N_2 specimens as compared to the Ar counterparts. Indeed, literature has reported as high as 7% percent of retained austenite in non-heat treated LB-PBF 17−4 PH SS fabricated in N_2 (this also depends on the powder atomization media, N_2 versus Ar). This work measured around 1% retained austenite via EBSD scan of a cross-sectioned plane (for Ar-atomized powder) consistently in non-heat treated and heat treated N_2 specimens. The higher ductility, in addition to the higher fraction of retained austenite, can be also ascribed to the smaller size and population of pores in the N_2 specimens. It has been reported for the LB-PBF 316 L that the ductility improved considerably by reducing the volumetric defects [56].

The slightly increased yield strength for both NHT-N_2 and HT-N_2 conditions as compared to their Ar counterparts can be generally attributed to the refined microstructure. For NHT specimens, the strength is expected to be governed by the Hall-Petch relation, where the strength is inversely related to grain size. While the reduction in grain size occurred in some regions for NHT-N_2 specimens, this does not lead to a substantial change in the yield strength, only ~15 MPa higher yield strength than the NHT-Ar specimens. For HT specimens, the improvement in yield strength as a result of using N_2 shield gas is slightly more notable (~ 28 MPa). This originates from a reduction in the martensitic lath thickness in the HT-N_2 specimens compared to the HT-Ar ones. Indeed, the ECCI micrographs presented in Fig. 10, comparing the thickness of lath martensite (yellow dashed arrows) for HT-N_2 and HT-Ar specimens, support this argument. As seen in Fig. 10(a), the HT-N_2 specimens have smaller martensite thickness (average of ~560 nm) as compared to that of HT-Ar ones in Fig. 10(b) (average of ~1400 nm). The fine grains formed after fabrication in the NHT-N_2 specimen (see Fig. 2(c)) transform to fine austenite grains during the CA heat treatment step (i.e. fine δ→ fine γ), which consequently influence the final laths martensite size upon quenching. Note that white particles are remnants of the polishing compound, not any secondary phases in the 17−4 PH SS, as confirmed by FIB surface polishing.

To elaborate, martensitic phases nucleated from the prior γ grains obeys the Kurdjumov-Sachs (K–S) orientation relation, i.e. $\{111\}_\gamma // \{110\}_{\alpha'}$ and $<110>_\gamma // <111>_{\alpha'}$. The habit plane of the γ-α' interface is always a {111} or a near- {111} plane. Since there are four sets of {111} planes in the FCC γ phase, the choice of these habit plane is always randomized [57]. After the γ→α' transformation, the prior γ grain is divided into "packets" of laths that share the same habit planes, and each packet is further subdivided into blocks (the group of laths with the same orientation). The size of the packets, blocks, and consequently, the laths are related to the prior γ grain size. The finer the prior γ grains are; the finer the packets, blocks, and laths are for the HT specimens [61,62]. As for NHT ones, the lath martensitic structure is unclear, as was reported by others [15], and quantification on the lath thickness is not meaningful.

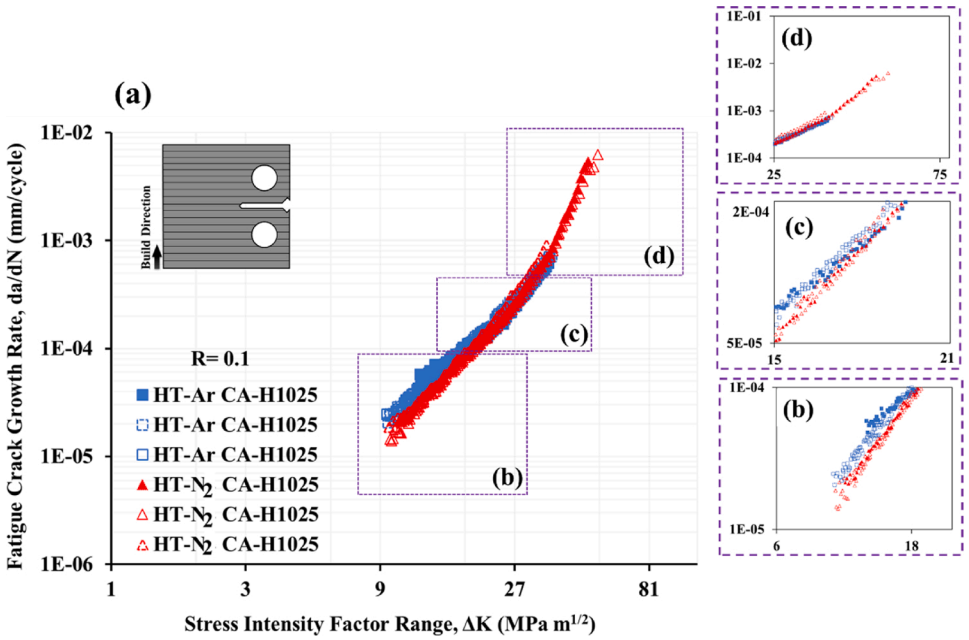

Fig. 7. Fatigue crack growth (FCG) rates for LB-PBF 17-4 PH SS specimens fabricated under N_2 and Ar shield gases in heat treated condition (CA-H1025). The three different FCG regimes (i.e. near threshold, Paris, and unstable FCG) are magnified and presented in (b), (c), and (d), respectively.

Table 5
Paris equation parameters based on best fit in the Paris regime for LB-PBF 17-4 PH SS specimens fabricated under N_2 and Ar shield gases.

	A (MPa. $m^{1/2}$)	n
HT-N_2	3.6×10^{-8}	2.7
HT-Ar	3.9×10^{-7}	2.1

It is, however, interesting to note that the true fracture stress of the HT-N_2 specimens is substantially lower than that of the HT-Ar specimens. This, again, maybe attributed to the substantially smaller martensite lath thicknesses (as low as ~200 nm) observed for the HT-N_2 specimens. At such small lath interface spacings, the mutual reactions and multiplications of dislocations are minimized, leading to low strain hardening capacity, and therefore, lower true fracture stress of the HT-N_2 specimens. In addition, it has been reported that the presence of retained austenite can attenuate the precipitation hardening effect.

4.2. Enhanced fatigue performance via in-process refinement of micro-/defect-structure

In general, defects such as surface roughness, LoF, pores, etc., compromise the fatigue performance of materials. In the case of machined specimens (i.e. absence of surface roughness), volumetric defects (i.e. pores, LoF defects, etc.) typically dominate the fatigue behavior [9,11]. The LoF defects in AM materials normally form when the ratio of overlap depth/layer thickness (d_0/t_L) is close to (or lower than 1), where the fusion of subsequent layers cannot occur successfully [11,12]. Referring to Fig. 4, the d_0/t_L ratio for both HT-N_2 and HT-Ar specimens is higher than 1, therefore, technically the possibility for formation of LoF defects is low in both conditions. However, the porosity size and distribution are different for HT-N_2 and HT-Ar specimens (see Fig. 5); the HT-N_2 specimens have fewer and smaller pores as compared to those of HT-Ar specimens. Accordingly, HT-N_2 specimens are expected to have higher fatigue resistance than HT-Ar ones, specifically in the HCF regime.

Fig. 9 shows that HT-N_2 specimens have slightly higher fatigue lives at 0.004 mm/mm strain amplitude. In this case, although the smaller pores in HT-N_2 specimens (see Fig. 5) may have delayed the crack

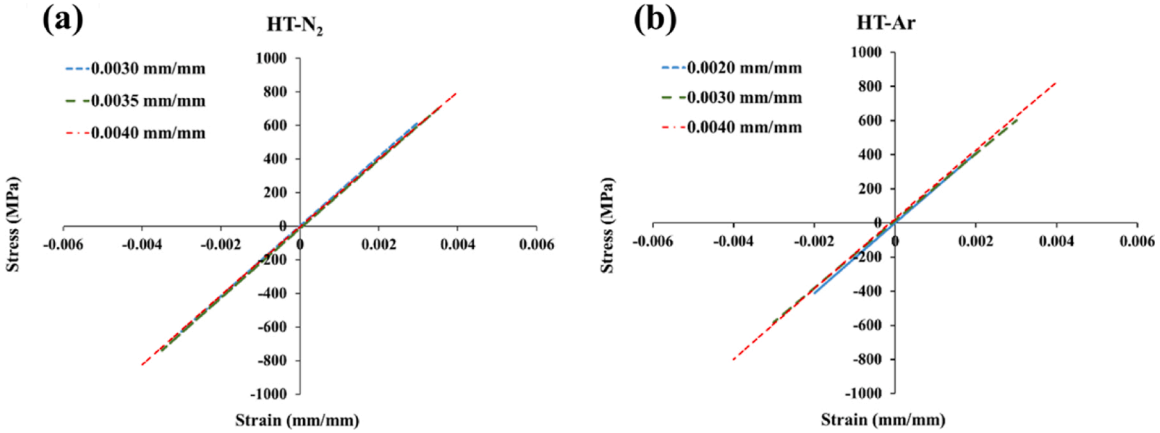

Fig. 8. Stable hysteresis loops of fully-reversed strain-controlled constant amplitude fatigue tests of LB-PBF 17-4 PH SS specimens: (a) HT-N_2, and (b) HT-Ar [6].

Table 6
Fully-reversed fatigue test results of LB-PBF 17-4 PH SS fabricated under N_2 and Ar [6] heat treated following CA-H1025 procedure.

	Specimen ID	ε_a (mm/mm)	σ_a (MPa)	σ_m (MPa)	$2N_f$ (Reversals)
HT-N_2	N1	0.0025	495	0	>11,000,000
	N11	0.0025	496	0	>11,000,000
	N2	0.0025	513	−1	10,825,018
	N4	0.0030	615	15	1,173,562
	N5	0.0030	609	−10	434,606
	N3	0.0030	622	5	305,686
	N7	0.0035	710	20	128,870
	N6	0.0035	720	19	123,384
	N8	0.0035	710	−2	122,300
	N10	0.0040	803	−6	77,218
	N9	0.0040	805	−12	65,948
HT-Ar	Ar1	0.0020	406	13	>11,000,000
	Ar2	0.0020	410	0	>11,000,000
	Ar12	0.0025	505	2	>11,000,000
	Ar3	0.0025	509	24	2,496,340
	Ar4	0.0025	506	23	1,394,730
	Ar11	0.0025	506	25	690,584
	Ar5	0.0030	604	−2	254,274
	Ar6	0.0030	593	9	244,684
	Ar7	0.0035	713	−12	135,110
	Ar8	0.0035	721	−9	121,066
	Ar9	0.0040	812	14	51,348
	Ar10	0.0040	809	24	39,764

initiation, a considerable portion of the fatigue life in the LCF regime is dominated by crack growth, in which regard the HT-N_2 only performed slightly better than HT-Ar specimens (lower FCG rates for HT-N_2 near threshold as well as in the Paris regime shown in Fig. 7). As such, there is only minimal improvement in fatigue resistance of these specimens observed.

In the HCF regime, as the majority of life is dominated by the initiation of fatigue cracks, the improvement in fatigue behavior of HT-N_2 specimens is mainly associated with its smaller and fewer pores as compared to those of the HT-Ar counterparts (Fig. 5). It has been shown for various AM material systems (e.g. Ti-6Al-4 V [63], AlSi10Mg [64], etc.) that the stress concentrations associated with pores are effective crack initiators and the internal pore size correlates well with the high cycle fatigue strength of the materials [65–68], i.e. fatigue life is shorter in the cases where the pores are larger.

In addition to volumetric defects, the surrounding microstructure may also influence the fatigue performance of AM materials. Indeed, the initiation and growth of microstructural small cracks are governed by slip and require a sufficient amount of plastic deformation which can be suppressed by refined microstructure. In wrought materials, the initiation and growth of microscopic cracks are generally delayed by refined grains, and the fatigue limits have been found to be inversely related to grain size [5]. With the presence of porosity induced stress concentration, similar arguments apply. For instance, enhancement in high cycle fatigue performance attributed to the fine grains around the defects has been reported for hot isostatic pressed (HIPed) LB-PBF Ti-6Al-4 V [69]. Similarly, in the case of LB-PBF 17−4 PH SS, the finer microstructure observed in HT-N_2 specimens (Fig. 2(c) and (e)) as compared to the HT-Ar specimens (Fig. 2(d) and (f)) can also provide additional fatigue resistance in the HCF regime.

Fig. 11 shows the fracture surfaces of specimens fabricated in Ar shield gas at 0.0025 mm/mm strain amplitude with different fatigue lives. Cracks are seen to initiate from pores close to the machined surface for all the specimens. More importantly, fatigue lives depend on the pore size, i.e. generally the smaller the pore, the longer the fatigue life [35]. For instance, for specimen "Ar3" with 2,496,340 reversals to failure (Fig. 11(a)), crack initiated from a pore close to the surface with the size of 18 μm, while the fatigue resistance decreased as the size of the pore increased to 31 μm (Fig. 11(b)) for specimen "Ar4" with 1,394,730 reversals to failure. It is worth noting that the edge is seen on the fracture surface close to the pore in Fig. 11(a) occurred due to the compression during the fully-reversed fatigue loading.

Fig. 11(c) shows the fracture surface of "Ar11″ with 690,584 reversals to failure. The crack initiated from two pores, one with the diameters of 37 μm and exposed to the surface, and the second with a diameter of 14 μm and very close to the surface. The reason for the shorter fatigue life obtained for this specimen as compared to previous cases (see Fig. 11(a) and (b)) is that the cracks were initiated from multiple pores on the surface of the specimen, in addition to one of these pores being relatively large compared to the crack initiating pores in other specimens. It has been reported that the mutual interaction of pores and pore-surface interaction induced stress concentrations may accelerate the initiation of the cracks [63,68,70,71].

Fig. 12 presents the fracture surface of LB-PBF 17−4 PH SS specimen fabricated under N_2 shield gas ("N2" specimen), which failed shortly after 10^7 cycles. It is of interest to investigate the crack initiation mechanism in this particular specimen, as two other tests in this strain

Table 7
Basquin equation (Eq. 2) fitting parameters for stress-life behavior of CA-H1025 LB-PBF 17-4 PH SS specimens fabricated under N_2 and Ar shield gases.

	σ'_f (MPa)	b	R^2
HT-N_2	1956	−0.085	0.88
HT-Ar	3269	−0.132	0.91

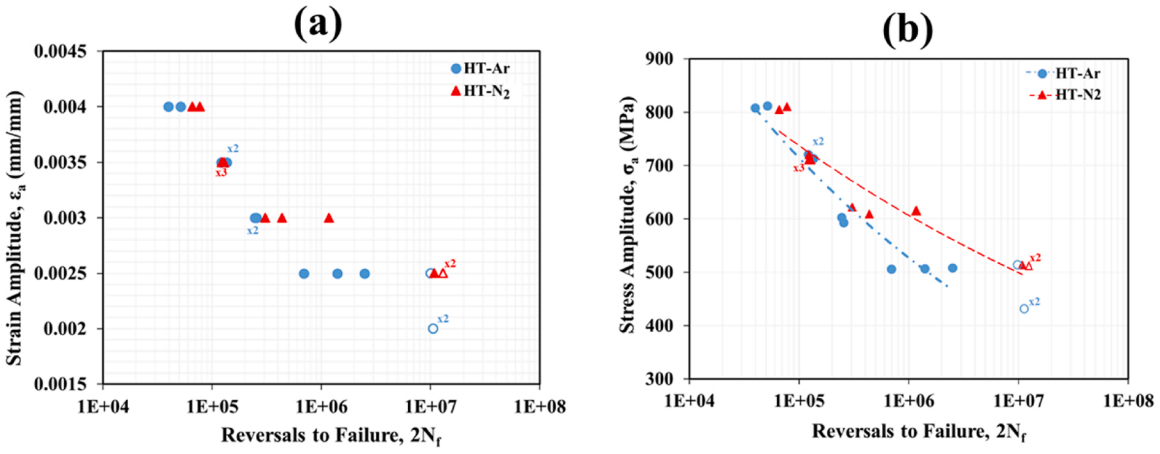

Fig. 9. (a) Strain-life and (b) stress-life fatigue data for CA-H1025 LB-PBF 17-4 PH SS representing the effect of shield gas type (N_2 vs. Ar [6]). Note that hallow marks represent the run-out tests.

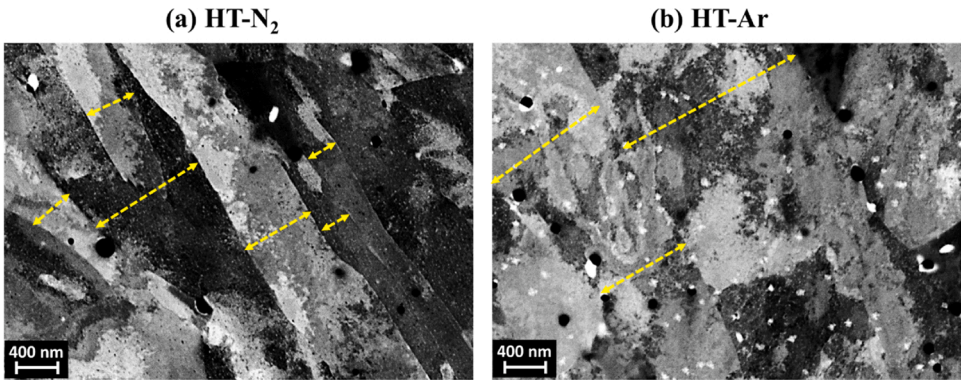

Fig. 10. The electron channeling contrast images (ECCI) of LB-PBF 17-4 PH SS showing the lath martensite in (a) HT-N_2, and (b) HT-Ar specimens. Note that the yellow dashed arrows are representing the lath martensite thickness. White particles are remnants of the polishing compound, not any secondary phases in the 17-4 PH SS, as confirmed by FIB surface polishing.

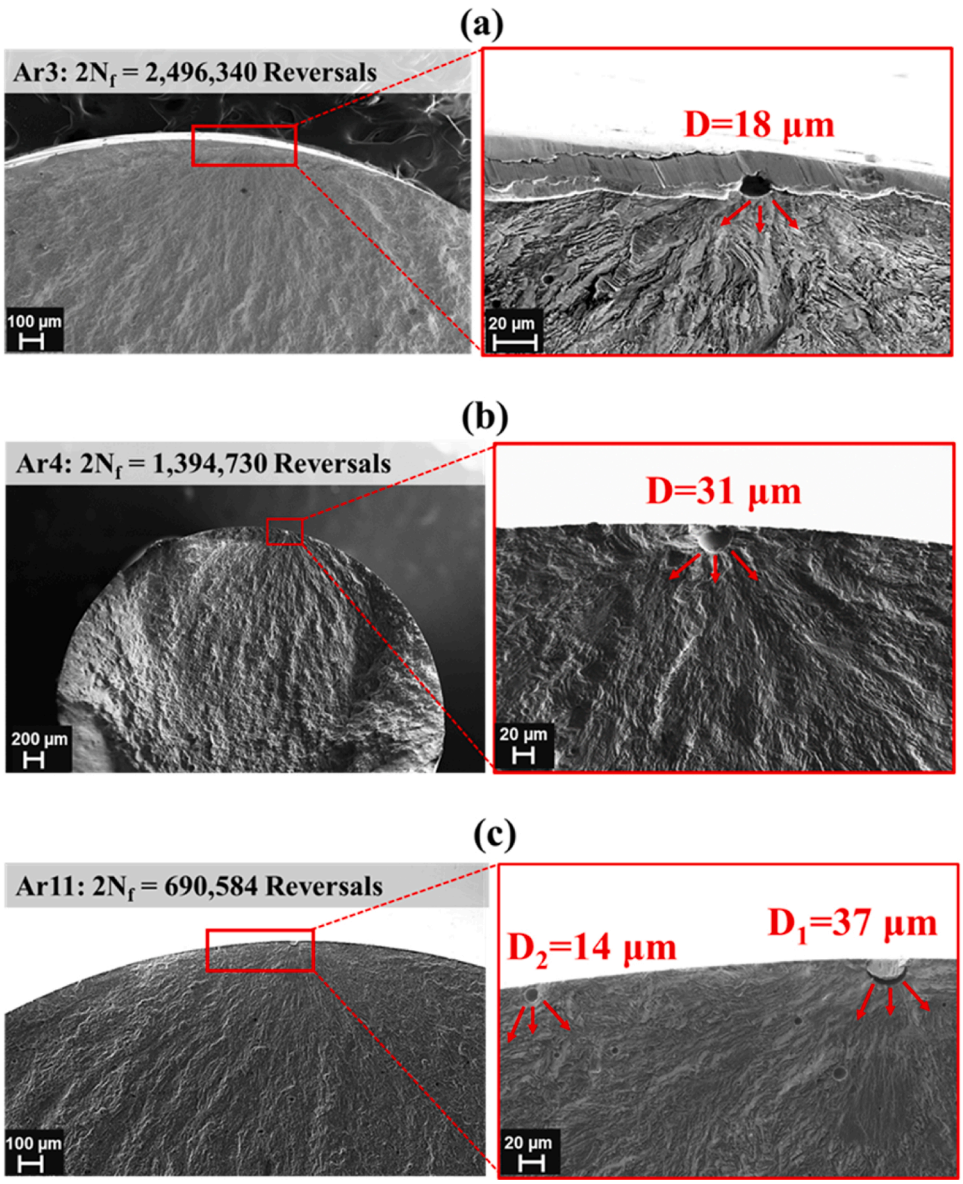

Fig. 11. Fracture surfaces of HT-Ar specimens at 0.0025 mm/mm strain amplitude: (a) specimen "Ar3" with 2,496,340 reversals to failure, (b) specimen "Ar4" with 1,394,730 reversals to failure, and (c) specimen "Ar11" with 690,584 reversals to failure.

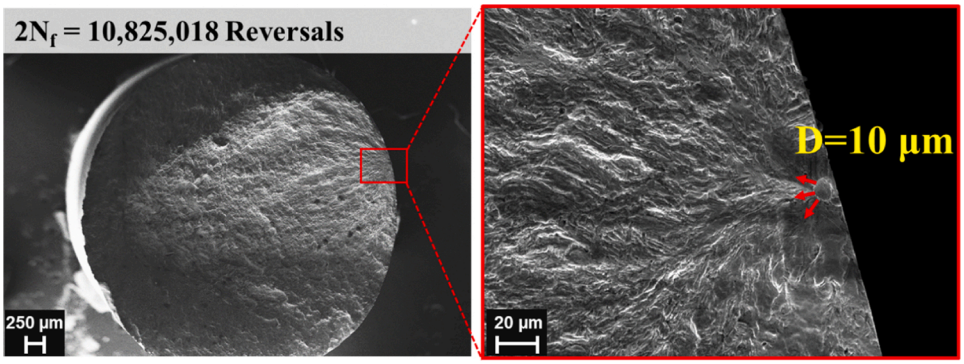

Fig. 12. Fracture surface of an LB-PBF 17-4 PH SS specimen fabricated under N_2 shield gas; specimen "N2" with 10,825,018 reversals to failure at 0.0025 mm/mm strain amplitude.

amplitude level did not fail within the tested period. For the "N2" specimen, the major crack was seen to have initiated from a pore close to the surface, with a diameter of 10 µm. The longer life observed in HT-N_2 specimens at 0.0025 mm/mm strain amplitude is attributed to the smaller pore as compared to the ones in Ar specimens seen in Fig. 11.

The smaller population of pores in N_2 specimens as compared to the Ar counterparts also reduces the chance for a pore to be exposed on (or very close to) the machined surface. To ensure the longer fatigue lives obtained for N_2 specimens as compared to the Ar ones are indeed the result of smaller pores, all fracture surfaces at various strain amplitudes were examined. It was observed that the crack initiating pores for N_2 specimens are all smaller than 20 µm, while the ones for Ar specimens range from 20 to 35 µm. It is postulated that the smaller pores in the N_2 specimens and the finer surrounding microstructure collectively resulted in a considerably better fatigue performance.

As seen in Fig. 7, the Ar specimens have inferior FCG resistance near threshold (Regime I), while exhibiting more or less identical FCG resistance toward the end of the Paris regime (Regime II) as compared to N_2 ones. The higher FCG resistance of N_2 specimens near the threshold region is due to the grain refinement observed in Fig. 2(c) and Fig. 10(a). It is well established that the growth of microstructurally small cracks is governed by slip and are along high Schmid-factor slip planes. Refined microstructure, therefore, retards the growth of these short cracks since it is typically associated with higher slip strengths [72,73]. Therefore, higher ΔK_{th} is expected for N_2 specimens as compared to that of Ar ones. To compare the stable crack growth mechanism of N_2 specimens with that of Ar ones, fractography analysis is carried out showing the role of grain refinement as well as the precipitation states in both conditions.

The fractography investigations of CT specimens at the Paris regime (i.e. Regime II) and Regime III are shown in Fig. 13(a) and (b) for HT-N_2 and HT-Ar specimens, respectively. It can be seen in fractography images for the Paris regime that crack growth appears to be a mixture of intergranular and intragranular modes (see the schematics embedded) and a 'sawtooth' feature is displaced (shown by double-side yellow arrows). The "grains" being referred here are the martensitic laths. Close inspection reveals that the size of the teeth correlates well with the

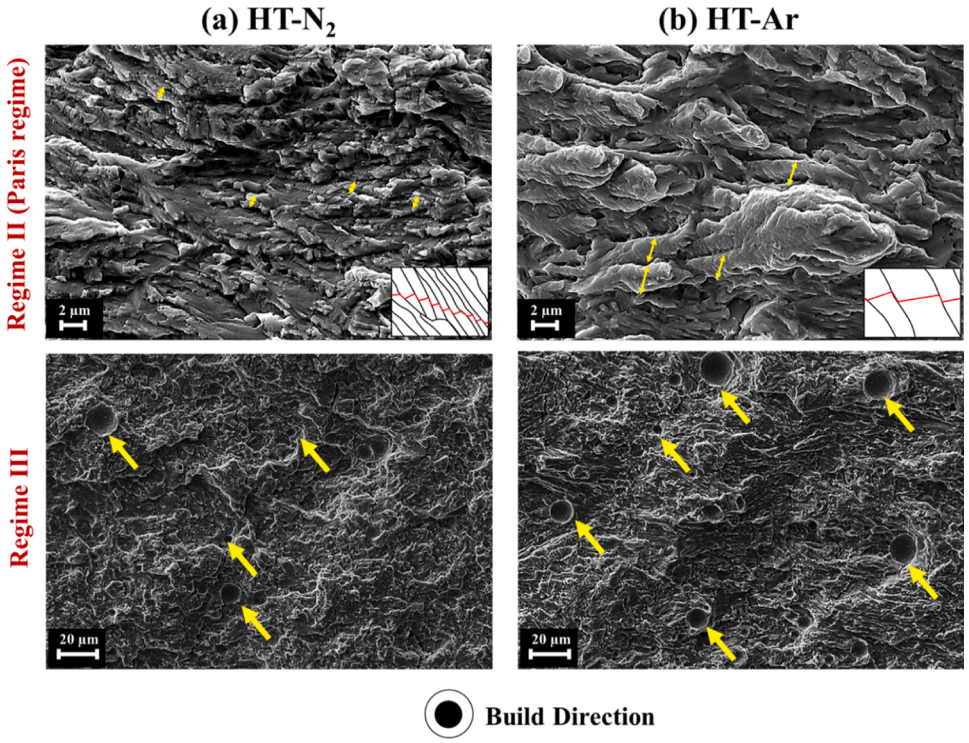

Fig. 13. Fractography of LB-PBF 17-4 PH SS CT specimens fabricated under different shield gas types and heat treated using CA-H1025 procedure: (a) HT-N_2 and (b) HT-Ar. The 'sawtooth' features are shown by double-side yellow arrows, and the exposed pores are indicated by yellow arrows. The schematics represent the laths martensite and how the crack is growing in the intergranular and intragranular modes.

thickness of the martensite laths in the two types of specimens. The sawtooth features are formed by crack growth and they are coarser for HT-Ar specimens (Fig. 13(b)) than HT-N_2 counterparts (Fig. 13(a)). This is ascribed to the difference in the microstructure of Ar and N_2 specimens. As shown in Fig. 10(b), HT-Ar specimens have coarser laths martensite (~1400 nm) as compared to HT-N_2 specimens (~560 nm), and it can be seen from Fig. 13 that the sawtooth's sizes are identical to the lath martensite thicknesses in both conditions. The average sawtooths' size measured in Fig. 13 for HT-Ar and HT-N_2 are 1500 nm and 600 nm, respectively. It is therefore inferred that the fatigue cracks grew along the lath martensite boundaries even in the long crack growth regime.

In Regime III, HT-N_2 specimens exhibit higher cyclic fracture toughness by tolerating higher ΔK values than the HT-Ar specimens, as seen in Fig. 7. Correspondingly, the fracture surfaces in this regime revealed far less and smaller pores for the HT-N_2 specimens (Fig. 13(a)) than for HT-Ar specimens (Fig. 13(b)). It is therefore apparent that the presence of a high fraction of defects (i.e. gas entrapped pores) in HT-Ar specimens decreases the material tolerance in the presence of a crack, resulting in an earlier fracture.

5. Conclusions

This study demonstrated an enhanced fatigue performance for LB-PBF 17−4 PH SS via in-process refinement of microstructure and defects using N_2 shield gas as an alternative to Ar. The effects of the shield gas on the microstructure, defects, fatigue crack initiation and growth behavior of LB-PBF 17−4 PH SS were investigated and presented. Based on the results obtained in this study, the following conclusions can be drawn:

1 The use of N_2 as the shield gas led to a finer microstructure containing more retained austenite as compared to specimens fabricated under Ar shield gas. This is attributed to the high solubility of N_2 in 17−4 PH SS and its austenite-stabilizing ability.
2 Islands of fine equiaxed grains observed close to the entrapped gas pores in the microstructure of N_2 specimens proved the fact that N_2 had diffused to the melt pool and prohibited grain growth.
3 The pores formed in N_2-shielded specimens were smaller both in size and in population. This is because the N_2 gas pores may, 1) be absorbed by the melt pool and dissolve in material shrinking the pore, or 2) escape the melt pool by either having more time during the slower solidification or by re-melting during printing the subsequent layer noting that melt pools of N_2 specimens were found to be deeper.
4 The N_2-shielded specimens possessed higher yield strength and ductility as compared to the Ar-shielded ones (for both non-heat treated and heat treated conditions). The higher ductility may be attributed to the lower internal defects as well as the presence of retained austenite, and the higher yield strength is ascribed to the fine equiaxed grains of N_2 specimens.
5 The finer lath martensite in HT-N_2 specimens decreased the potential for strain hardening of the material, and resulted in lower true fracture stress as compared to the HT-Ar counterparts.
6 Axial fatigue performance of LB-PBF 17−4 PH SS was increased moderately in low cycle fatigue, and considerably in high cycle fatigue regime when N_2 was used as the shield gas. The improvement in fatigue resistance of LB-PBF 17−4 PH SS fabricated under N_2 shield gas was attributed to the refined micro-/defect-structure.
7 Using N_2 as shield gas resulted in a moderately lower FCG rate for LB-PBF 17−4 PH SS in a wide range of ΔK levels (including the near-threshold regime and the Paris regime) as compared to the condition where Ar was used as the shield gas. This can be attributed to the grain refinement (i.e. islands of fine equiaxed grains) effects. Ar specimens have lower cyclic fracture toughness, which is due to the larger and more pores in the specimens.

CRediT authorship contribution statement

P.D. Nezhadfar: Conceptualization, Methodology, Validation, Formal analysis, Data curation, Investigation, Writing - original draft, Visualization. **Kathryn Anderson-Wedge:** Investigation, Validation, Data curation. **S.R. Daniewicz:** Resources, Investigation, Validation, Data curation. **Nam Phan:** Conceptualization, Funding acquisition, Writing - review & editing. **Shuai Shao:** Conceptualization, Validation, Formal analysis, Investigation, Writing - review & editing, Visualization. **Nima Shamsaei:** Conceptualization, Methodology, Resources, Formal analysis, Investigation, Writing - review & editing, Supervision, Project administration.

Declaration of Competing Interest

The authors declare that they have no known competing financial interests or personal relationships that could have appeared to influence the work reported in this paper.

References

[1] T. DebRoy, H.L. Wei, J.S. Zuback, T. Mukherjee, J.W. Elmer, J.O. Milewski, A. M. Beese, A. Wilson-Heid, A. De, W. Zhang, Additive manufacturing of metallic components – process, structure and properties, Prog. Mater. Sci. 92 (2018) 112–224.
[2] N. Shamsaei, A. Yadollahi, L. Bian, S.M. Thompson, An overview of direct laser deposition for additive manufacturing; Part II: mechanical behavior, process parameter optimization and control, Addit. Manuf. 8 (2015) 12–35.
[3] Y. Kok, X.P. Tan, P. Wang, M.L.S. Nai, N.H. Loh, E. Liu, S.B. Tor, Anisotropy and heterogeneity of microstructure and mechanical properties in metal additive manufacturing: a critical review, Mater. Des. 139 (2018) 565–586.
[4] Y.J. Liu, Z. Liu, Y. Jiang, G.W. Wang, Y. Yang, L.C. Zhang, Gradient in microstructure and mechanical property of selective laser melted AlSi10Mg, J. Alloys. Compd. 735 (2018) 1414–1421.
[5] R.I. Stephens, A. Fatemi, R.R. Stephens, H.O. Fuchs, Metal Fatigue in Engineering, John Wiley & Sons, 2000.
[6] P.D. Nezhadfar, R. Shrestha, N. Phan, N. Shamsaei, Fatigue behavior of additively manufactured 17-4 PH stainless steel: synergistic effects of surface roughness and heat treatment, Int. J. Fatigue 124 (2019) 188–204.
[7] A.J. Sterling, B. Torries, N. Shamsaei, S.M. Thompson, D.W. Seely, Fatigue behavior and failure mechanisms of direct laser deposited Ti–6Al–4V, Mater. Sci. Eng. A 655 (2016) 100–112.
[8] A. Fatemi, R. Molaei, J. Simsiriwong, N. Sanaei, J. Pegues, B. Torries, N. Phan, N. Shamsaei, Fatigue behaviour of additive manufactured materials: an overview of some recent experimental studies on Ti-6Al-4V considering various processing and loading direction effects, Fatigue Fract. Eng. Mater. Struct. 42 (2019) 991–1009.
[9] A. Yadollahi, N. Shamsaei, Additive manufacturing of fatigue resistant materials: challenges and opportunities, Int. J. Fatigue 98 (2017) 14–31.
[10] S.R. Daniewicz, N. Shamsaei, An introduction to the fatigue and fracture behavior of additive manufactured parts, Int. J. Fatigue 94 (2017) 167.
[11] R. Shrestha, N. Shamsaei, M. Seifi, N. Phan, An investigation into specimen property to part performance relationships for laser beam powder bed fusion additive manufacturing, Addit. Manuf. 29 (2019).
[12] NASA, MSFC-SPEC-3717 - Specification for Control and Qualification of Laser Powder Bed Fusion Metallurgical Processes, 2017, p. 58.
[13] L. Facchini, N. Vicente, I. Lonardelli, E. Magalini, P. Robotti, A. Molinari, Metastable Austenite in 17-4 precipitation-hardening stainless steel produced by selective laser melting, Adv. Eng. Mater. 12 (2010) 184–188.
[14] G.V. Kurdjumov, A.G. Khachaturyan, Phenomena of carbon atom redistribution in martensite, Metall. Trans. 3 (1972) 1069–1076.
[15] M. Alnajjar, F. Christien, K. Wolski, C. Bosch, Evidence of austenite by-passing in a stainless steel obtained from laser melting additive manufacturing, Addit. Manuf. 25 (2019) 187–195.
[16] S. Cheruvathur, E.A. Lass, C.E. Campbell, Additive manufacturing of 17-4 PH stainless steel: post-processing heat treatment to achieve uniform reproducible microstructure, Jom 68 (2015) 930–942.
[17] P.D. Nezhadfar, E. Burford, K. Anderson-Wedge, B. Zhang, S. Shao, S.R. Daniewicz, N. Shamsaei, Fatigue crack growth behavior of additively manufactured 17-4 PH stainless steel: effects of build orientation and microstructure, Int. J. Fatigue 123 (2019) 168–179.
[18] S. Vunnam, A. Saboo, C. Sudbrack, T.L. Starr, Effect of powder chemical composition on the as-built microstructure of 17-4 PH stainless steel processed by selective laser melting, Addit. Manuf. (2019), 100876.
[19] P.D. Nezhadfar, A. Soltani-Tehrani, A. Sterling, N. Tsolas, N. Shamsaei, The effects of powder recycling on the mechanical properties of additively manufactured 17-4 PH stainless steel, Proc. 29th Annu. Int. Solid Free. Fabr. Symp. – An Addit. Manuf. Conf. (2018) 1292–1300.

[20] A. Soltani-Tehrani, J. Pegues, N. Shamsaei, Fatigue behavior of additively manufactured 17-4 PH stainless steel: the effects of part location and powder re-use, Addit. Manuf. 33 (2020).
[21] S. Pasebani, M. Ghayoor, S. Badwe, H. Irrinki, S.V. Atre, Effects of atomizing media and post processing on mechanical properties of 17-4 PH stainless steel manufactured via selective laser melting, Addit. Manuf. 22 (2018) 127–137.
[22] H. Gu, H. Gong, D. Pal, K. Rafi, T. Starr, B. Stucker, Influences of energy density on porosity and microstructure of selective laser melted 17-4PH stainless steel, in: Solid Free. Fabr. 2013 Proc. 23rd Annu. Int. Solid Free. Fabr. Symp. – An Addit. Manuf. Conf., Austing, TX, 2013, 2013.
[23] R. Shrestha, P.D. Nezhadfar, M. Masoomi, J. Simsiriwong, N. Pham, N. Shamsaei, Effects of design parameters on thermal history and mechanical behavior of additively manufactured 17-4 PH stainless steel, Proc. 29th Annu. Int. Solid Free. Fabr. Symp. – An Addit. Manuf. Conf. (2018).
[24] P.D. Nezhadfar, M. Masoomi, S.M. Thompson, N. Phan, N. Shamsaei, Mechanical properties of 17-4 PH stainless steel additively manufactured under Ar and N2 shielding gas, in: Proc. 29th Annu. Int. Solid Free. Fabr. Symp. – An Addit. Manuf. Conf., Austing, TX, 2018, pp. 1301–1310.
[25] A. Ladewig, G. Schlick, M. Fisser, V. Schulze, U. Glatzel, Influence of the shielding gas flow on the removal of process by-products in the selective laser melting process, Addit. Manuf. 10 (2016) 1–9.
[26] L.E. Murr, E. Martinez, K.N. Amato, S.M. Gaytan, J. Hernandez, D.A. Ramirez, P. W. Shindo, F. Medina, R.B. Wicker, Fabrication of metal and alloy components by additive manufacturing: examples of 3D materials science, J. Mater. Res. Technol. 1 (2012) 42–54.
[27] M.B. Mathisen, H.L. Larsen, Solidification Refinement and General Phase Transformation Control Through Application of Insitu Gas Jet Impingement in Metal Additive Manufacturing, 2019.
[28] T.L. Starr, K. Rafi, B. Stucker, C.M. Scherzer, Controlling phase composition in selective laser melted stainless steels, Power (W) 195 (2012) 195.
[29] T. LeBrun, T. Nakamoto, K. Horikawa, H. Kobayashi, Effect of retained austenite on subsequent thermal processing and resultant mechanical properties of selective laser melted 17–4 PH stainless steel, Mater. Des. 81 (2015) 44–53.
[30] L.E. Murr, E. Martinez, J. Hernandez, S. Collins, K.N. Amato, S.M. Gaytan, P. W. Shindo, Microstructures and properties of 17-4 PH stainless steel fabricated by selective laser melting, J. Mater. Res. Technol. 1 (2012) 167–177.
[31] P. Kah, J. Martikainen, Influence of shielding gases in the welding of metals, Int. J. Adv. Manuf. Technol. 64 (2013) 1411–1421.
[32] M. Keskitalo, K. Mäntyjärvi, J. Sundqvist, J. Powell, A.F.H. Kaplan, Laser welding of duplex stainless steel with nitrogen as shielding gas, J. Mater. Process. Technol. 216 (2015) 381–384.
[33] M. Keskitalo, J. Sundqvist, K. Mäntyjärvi, J. Powell, A.F.H. Kaplan, The influence of shielding gas and heat input on the mechanical properties of laser welds in ferritic stainless steel, Phys. Procedia 78 (2015) 222–229.
[34] N. Seto, S. Katayama, A. Matsunawa, High-speed simultaneous observation of plasma and keyhole behavior during high power CO2 laser welding: effect of shielding gas on porosity formation, J. Laser Appl. 12 (2000) 245–250.
[35] J. Sun, P. Nie, K. Feng, Z. Li, B. Guo, E. Jiang, The elimination of pores in laser welds of AISI 304 plate using different shielding gases, J. Mater. Process. Technol. 248 (2017) 56–63.
[36] A.M. Meyer, M.D. Toit, Interstitial diffusion of carbon and nitrogen into heat-affected zones of 11-12% chromium steel welds, Weld. J. N.Y. 80 (2001), 275-s.
[37] P. Bajaj, A. Hariharan, A. Kini, P. Kürnsteiner, D. Raabe, E.A. Jägle, Steels in additive manufacturing: a review of their microstructure and properties, Mater. Sci. Eng. A (2019), 138633.
[38] M. Song, R. Zhou, J. Gu, Z. Wang, S. Ni, Y. Liu, Nitrogen induced heterogeneous structures overcome strength-ductility trade-off in an additively manufactured high-entropy alloy, Appl. Mater. Today 18 (2020), 100498.
[39] S. Katayama, Y. Kawahito, M. Mizutani, Elucidation of laser welding phenomena and factors affecting weld penetration and welding defects, Phys. Procedia 5 (2010) 9–17.
[40] J. Ahn, E. He, L. Chen, J. Dear, C. Davies, The effect of Ar and He shielding gas on fibre laser weld shape and microstructure in AA 2024-T3, J. Manuf. Process. 29 (2017) 62–73.
[41] J.W. Elmer, J. Vaja, H.D. Carlton, R. Pong, The effect of Ar and N2 shielding gas on laser weld porosity in steel, stainless steels, and nickel, Weld. J. 94 (2015) 313s–325s.
[42] R. Akhter, M. Davis, J. Dowden, P. Kapadia, M. Ley, W.M. Steen, A method for calculating the fused zone profile of laser keyhole welds, J. Phys. D Appl. Phys. 22 (1989) 23–28.
[43] P. Behjati, A. Kermanpur, A. Najafizadeh, H. Samaei Baghbadorani, L. P. Karjalainen, J.G. Jung, Y.K. Lee, Effect of nitrogen content on grain refinement and mechanical properties of a reversion-treated Ni-Free 18Cr-12Mn austenitic stainless steel, Metall. Mater. Trans. A 45 (2014) 6317–6328.
[44] A. Di Schino, M. Barteri, J.M. Kenny, Effects of grain size on the properties of a low nickel austenitic stainless steel, J. Mater. Sci. 38 (2003) 4725–4733.
[45] Y. Kawahito, M. Mizutani, S. Katayama, High quality welding of stainless steel with 10 kW high power fibre laser, Sci. Technol. Weld. Join. 14 (2009) 288–294.
[46] R.O. Ritchie, A.W. Thompson, On macroscopic and microscopic analyses for crack initiation and crack growth toughness in ductile alloys, Metall. Trans. A (1985).
[47] ASTM E647, Standard Test Method for Measurement of Fatigue Crack Growth Rates, 2016.
[48] ASTM E3-11, Standard Guide for Preparation of Metallographic Specimens, 2017.
[49] ASTM E606/E606M−12, Standard Test Method for Strain-controlled Fatigue Testing, ASTM Int., 2012.
[50] S. Hertzman, M. Jarl, A Thermodynamic Analysis of the Fe-Cr-N System, n.d.
[51] P. Sathiya, M.Y.A. Jaleel, Influence of shielding gas mixtures on bead profile and microstructural characteristics of super austenitic stainless steel weldments by laser welding, Int. J. Adv. Manuf. Technol. (2011).
[52] A.M. Galloway, N.A. McPherson, T.N. Baker, An evaluation of weld metal nitrogen retention and properties in 316LN austenitic stainless steel, Proc. Inst. Mech. Eng. Part L J. Mater. Des. Appl. 225 (2011) 61–69.
[53] R.K. Okagawa, R.D. Dixon, D.L. Olson, The influence of nitrogen from welding on stainless steel weld metal microstructures soluble nitrogen is found to exert a major influence-particularly on the quantity and distribution of weld metal delta ferrite, Weld. Res. Suppl. (1983) 204s–209s.
[54] S. Tammas-Williams, H. Zhao, F. Léonard, F. Derguti, I. Todd, P.B. Prangnell, XCT analysis of the influence of melt strategies on defect population in Ti–6Al–4V components manufactured by selective electron beam melting, Mater. Charact. 102 (2015) 47–61.
[55] ASTM A693-16, Standard Specification for Precipitation-hardening Stainless and Heat-resisting Steel Plate, Sheet, and Strip, ASTM Int., 2016.
[56] P.D. Nezhadfar, A. Soltani-Tehrani, N. Shamsaei, Effect of preheating build platform on microstructure and mechanical properties of additively manufactured 316L stainless steel, Proc. 30th Annu. Int. Solid Free. Fabr. Symp. – An Addit. Manuf. Conf. (2019).
[57] E. Pereloma, D.V. Edmonds, Phase transformations in steels 2: diffusionless transformations, high strength steels. Modelling and Advanced Analytical Techniques, Woodhead Publishing, 2012.
[58] M. Moallemi, A. Zarei-Hanzaki, S.-J. Kim, C. Hong, P.D. Nezhadfar, Deformation behavior of a high-plasticity nano/ultrafine-grained N-bearing duplex stainless steel: twin/twin-like induced plasticity effect, Mater. Sci. Eng. A 700 (2017).
[59] R. Manojkumar, S. Mahadevan, C.K. Mukhopadhyay, B.P.C. Rao, Aging behavior of 17-4 PH stainless steel studied using XRDLPA for separating the influence of precipitation and dislocations on microstrain, J. Mater. Res. 32 (2017) 4263–4271.
[60] G.E. Dieter, Mechanical Metallurgy, 3rd ed., McGraw-Hill, Boston, MA, MA, 1986.
[61] F. Khodabakhshi, M.H. Farshidianfar, A.P. Gerlich, M. Nosko, V. Trembošová, A. Khajepour, Effects of laser additive manufacturing on microstructure and crystallographic texture of austenitic and martensitic stainless steels, Addit. Manuf. 31 (2020), 100915.
[62] S. Morito, H. Saito, O.T. Furuhara, T. Maki, Effect of austenite grain size on the morphology and crystallography of lath martensite in low carbon steels, ISIJ Int. 45 (2005) 91–94.
[63] S. Tammas-Williams, P.J. Withers, I. Todd, P.B. Prangnell, The influence of porosity on fatigue crack initiation in additively manufactured titanium components, Sci. Rep. 7 (2017).
[64] S. Romano, A. Abel, J. Gumpinger, A.D. Brandão, S. Beretta, Quality control of AlSi10Mg produced by SLM: metallography versus CT scans for critical defect size assessment, Addit. Manuf. 28 (2019) 394–405.
[65] R. Molaei, A. Fatemi, N. Sanaei, J. Pegues, N. Shamsaei, S. Shao, P. Li, D.H. Warner, N. Phan, Fatigue of additive manufactured Ti-6Al-4V, Part II: the relationship between microstructure, material cyclic properties, and component performance, Int. J. Fatigue 132 (2020), 105363.
[66] M. Tang, P.C. Pistorius, Oxides, porosity and fatigue performance of AlSi10Mg parts produced by selective laser melting, Int. J. Fatigue 94 (2017) 192–201.
[67] J.W. Pegues, S. Shao, N. Shamsaei, N. Sanaei, A. Fatemi, D.H. Warner, P. Li, N. Phan, Fatigue of additive manufactured Ti-6Al-4V, Part I: the effects of powder feedstock, manufacturing, and post-process conditions on the resulting microstructure and defects, Int. J. Fatigue 132 (2020), 105358.
[68] S. Romano, P.D. Nezhadfar, N. Shamsaei, M. Seifi, S. Beretta, High cycle fatigue behavior and life prediction for additively manufactured 17-4 PH stainless steel: effect of sub-surface porosity and surface roughness, Theor. Appl. Fract. Mech. 106 (2020), 102477.
[69] P. Li, D.H. Warner, J.W. Pegues, M.D. Roach, N. Shamsaei, N. Phan, Investigation of the mechanisms by which hot isostatic pressing improves the fatigue performance of powder bed fused Ti-6Al-4V, Int. J. Fatigue 120 (2019) 342–352.
[70] Z. Xu, W. Wen, T. Zhai, Effects of pore position in depth on stress/strain concentration and fatigue crack initiation. Metall. Mater. Trans. A Phys. Metall. Mater. Sci., 2012, pp. 2763–2770.
[71] S. Beretta, S. Romano, A comparison of fatigue strength sensitivity to defects for materials manufactured by AM or traditional processes, Int. J. Fatigue 94 (2017) 178–191.
[72] D. Kumar, S. Idapalapati, W. Wang, S. Narasimalu, Effect of surface mechanical treatments on the microstructure-property-performance of engineering alloys, Materials (Basel) 12 (2019).
[73] D. Wilson, F.P.E. Dunne, A mechanistic modelling methodology for microstructure-sensitive fatigue crack growth, J. Mech. Phys. Solids 124 (2019) 827–848.